Effect of temperature on deformation mechanisms of AZ31 Mg-alloy under tensile loading

Thibaut Dessolier, Pierre Lhuissier, Francine Roussel-Dherbey, Frédéric Charlot, Charles Josserond, Jean-Jacques Blandin, Guilhem Martin

To cite this version:

Thibaut Dessolier, Pierre Lhuissier, Francine Roussel-Dherbey, Frédéric Charlot, Charles Josserond, et al.. Effect of temperature on deformation mechanisms of AZ31 Mg-alloy under tensile loading. Materials Science and Engineering: A, 2020, 775, pp.138957. ⟨10.1016/j.msea.2020.138957⟩. ⟨hal-02952190⟩

HAL Id: hal-02952190

https://hal.science/hal-02952190v1

Submitted on 29 Sep 2020

Effect of Temperature on Deformation Mechanisms of AZ31 Mg-alloy under tensile loading

Thibaut Dessolier[1], Pierre Lhuissier[1], Francine Roussel-Dherbey[2],
Frédéric Charlot[2], Charles Josserond[1], Jean-Jacques Blandin[1], Guilhem Martin[1#]

1. Univ. Grenoble Alpes, CNRS, Grenoble INP, SIMaP, F-38000 Grenoble, France
2. Consortium des Moyens Technologiques Communs (CMTC) - Grenoble INP - Université Grenoble Alpes, BP 75, 38402 St Martin d'Hères, France

Corresponding Author:
Email: guilhem.martin@simap.grenoble-inp.fr

Abstract

Controlled in situ SEM tensile tests have been carried out between 200 and 300°C at a constant strain rate of 5.10^{-5} s^{-1} to investigate the effect of temperature on deformation mechanisms operating in an Mg-3Al-1Zn (AZ31) Mg-alloy. Fiducial microgrids deposited using electron beam lithography are used to evidence grain boundary sliding as well as to determine the spatial strain heterogeneities as a function of temperature. Dislocation creep and grain boundary sliding coexist between 200 and 300°C but their respective activity varies significantly as shown by the strain rate sensitivity value *m* which is about 0.2 at 200°C but about 0.5 at both 250 and 300°C. In addition, grain boundary sliding becomes predominant at 250 and 300°C whereas its occurrence is relatively limited at 200°C. Slip trace analysis shows that at 200°C prism and pyramidal <c+a> slip already exhibit a great activity. Spatial strain heterogeneities determined by digital image correlation (DIC) based on microgrid displacements develop during the early stage of plastic deformation and persist at larger strains. It is shown that the strain in the vicinity of grain boundaries intensifies when the temperature rises from 200 to 300°C while the core of grains accommodates less deformation in agreement with the fact that grain boundary sliding is predominant at 250 and 300°C.

Keywords: In situ; Magnesium alloys; SEM; Digital Image Correlation; High-temperature

1. Introduction

Despite their low density, the use of conventional magnesium alloys in the industry remains limited, in particular, due to their poor workability at room temperature (RT) associated with the hexagonal close-packed structure. At RT, Mg alloys deform plastically mainly by dislocation glide on the basal plane and twinning, limiting their ductility. This lack of ductility can be accounted for by the fact that the aforementioned deformation mechanisms do not allow to accommodate strains along the c-axis. In addition, wrought Mg-alloys, typically the AZ-series, exhibit strong basal textures, leading to significant anisotropy, i.e. Lankford coefficient can reach 4 or more, see e.g. [1,2]. When the temperature increases beyond 150°C, twinning activity vanishes and additional slip systems, namely prism and pyramidal <c+a> slips become easier to operate, see [3–6][7] among others. This results in a great improvement of the deformability that goes along with a reduced plastic anisotropy, see e.g. [2,8]. Finally, for alloys exhibiting relatively fine grains, typically less than 20 µm, grain boundary sliding can play a key role which results in an increase of the strain rate sensitivity parameter ($m = \partial\sigma/\partial\varepsilon$) and, in some cases, in superplastic properties. Superplasticity of Mg-alloys has been widely reported and studied, see e.g. [9–12][13]. Cavitation, identified as the damage mechanism in superplastic conditions has also received attention from the community [14][15].

Nevertheless, the detailed effect of temperature on plastic deformation of Mg-alloys remains an open question and is still debated. In particular, the simultaneous activation of various deformation mechanisms as well as data related to microscale plastic strain distribution with temperature in Mg-alloys are not yet fully available and would deserve to be deeply investigated. A path to provide new insights regarding the effect of temperature on the plastic strain distribution in Mg-alloys can be to carry out highly-controlled mechanical tests including continuous strain mapping by Digital Image Correlation (DIC). At RT, recent work has contributed to determine local strain fields and the associated deformation mechanisms, see in particular [16–18]. However, running such mechanical tests at high temperatures (here >200°C) is not an easy task. First Mg-alloys are prone to oxidation at high temperature, hence continuous imaging of the surface for further DIC analyses requires to work under vacuum. In situ mechanical tests within the SEM fulfills such a requirement but due to its low vapor pressure Mg might easily evaporate during high temperature (T >250°C) mechanical testing which can cause severe damage to the SEM. Finally, achieving a good control of the temperature when straining the sample during in situ tensile tests remains a challenge that needs to be overcome. For all these reasons, investigating high-temperature deformation of Mg-alloys using DIC during in situ SEM tensile tests is poorly documented, only some attempts to determine high-temperature strain fields can be found in [2]. Most of the studies employing DIC to investigate the deformation behavior of Mg-alloys have been conducted at RT [16–19]. A recent study by Orozco-Caballero et al. [16] has shown how magnesium accommodates local deformation incompatibility at RT relying on HR-DIC. Note that in the present work, we did not use HR-DIC but we rather use fiducial microgrids allowing to reveal the occurrence of grain boundary sliding when this mechanism becomes predominant in superplastic conditions.

In the present work, highly controlled high temperature in situ tensile tests including DIC were performed in an SEM (controlled temperature within ±5°C and controlled strain rate, see details in [20]). Particular attention was given (i) to the identification of deformation mechanisms as revealed by fiducial microgrids and slip trace analysis; and (ii) to the extent of strain localization through the microstructure as a function of temperature.

2. Experimental Procedures

2.1. Materials and specimen preparation

The as-received material was a commercial AZ31 Mg-alloy (3wt%Al-1wt%Zn-0.4wt%Mn) hot-rolled sheet with an initial thickness of 2 mm supplied by Satzgitter

Magnesium Technology GmbH. The hot-rolled sheet was annealed at 345°C for 1 h to achieve the "O" metallurgical state.

Samples were mechanically ground and polished using diamond (3 and 1µm) and alumina (0.3 µm) suspensions. A final electro-polishing stage in a solution consisting of phosphoric acid (60%) and ethanol (40%) at 20°C under 3V for 30 minutes was required to make the surface suitable for further EBSD measurements. The as-received microstructure was preliminarily characterized by EBSD in a ZEISS ULTRA 55 FEG-SEM equipped by a HIKARI PRO CCD camera from EDAX. Maps were acquired using an acceleration voltage of 20 kV and the high current mode with a step size of 0.2 µm. The initial microstructure was fully recrystallized with an average grain size of 12 ± 4µm, calculated based on the surface fraction definition, see **Figure 1a**. The average grain size was systematically estimated based on this definition throughout this manuscript. As usually observed in wrought AZ31 products, a strong basal texture was observed, the c-axis of the hexagonal lattice being oriented along the ND-direction as indicated in **Figure 1b**. Note that a slightly larger spread along the RD-direction than in the TD-direction was detected.

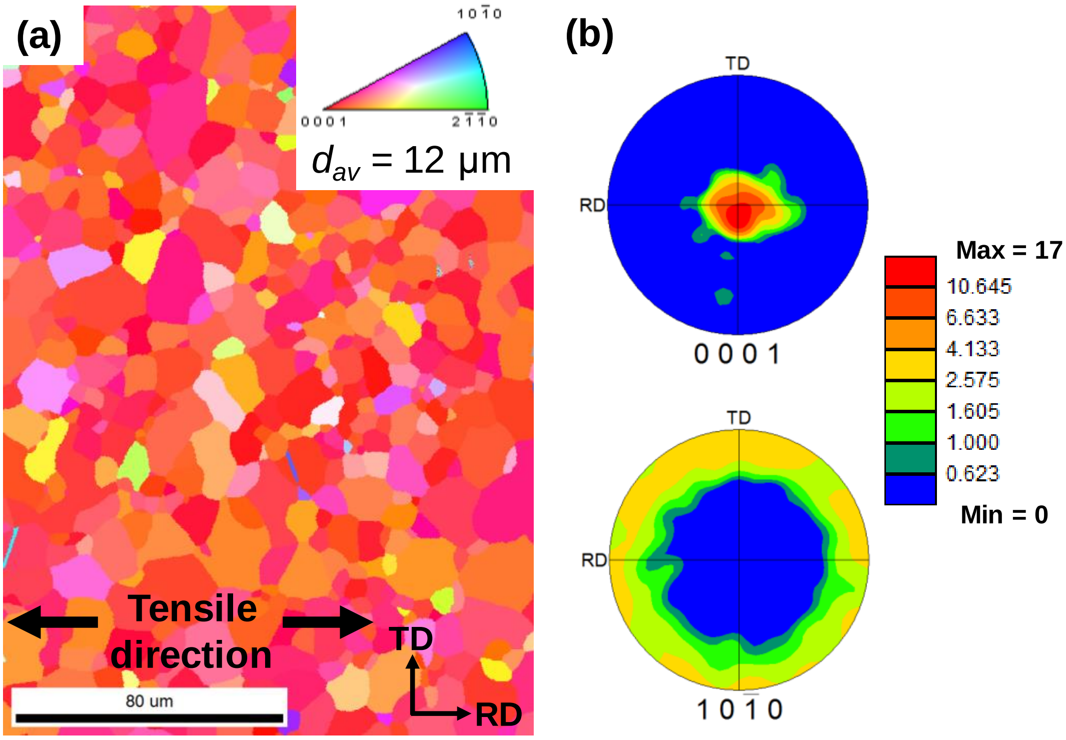

Figure 1. (a) EBSD IPF-ND map and (b) {0001} and {10-10} Pole Figures of the as-received AZ31 hot rolled sheet. Tensile direction is parallel to RD.

2.2. *High temperature in situ SEM controlled tensile tests*

A key point of the present investigation is to be able to conduct controlled high temperature tensile tests within the SEM. A lot of efforts have been made in order to achieve good temperature control, typically ±5°C as well as a strain rate control instead of a displacement rate control because it is much more relevant when studying the visco-plastic regime. A detailed description of the procedures developed to run high-temperature tests with a high degree of control is given in **Appendix A** and was already partly reported in [20].

In situ high-temperature tensile tests were carried out at 200, 250 and 300°C at a constant strain rate of 5.10^{-5} s^{-1}. The tensile direction was parallel to the rolling direction (RD). Higher temperatures were not considered due to the risk of Mg-evaporation. Because one the objective of the present work is to investigate the changes induced when switching from a deformation regime governed by dislocation creep to a superplastic regime governed by grain boundary sliding, the strain rate was deliberately chosen to make sure the material undergoes superplastic deformation at 300°C but not at 200°C. In order to ensure that a switch in predominant deformation mechanism occurs in the range of temperature investigated, i.e. 200-300°C, the strain rate was selected based on the Zener-Hollomon parameter ($Z = \dot{\varepsilon} \exp(Q / RT)$), with $\dot{\varepsilon}$ the strain rate and Q the activation energy). Using literature data [15] reporting the high temperature tensile mechanical behavior of the exact same fine grained AZ31 alloy under various temperatures and strain rates, we have first estimated the Z-parameter. Thus we got typical values of the Z-parameter when the deformation is governed by dislocation creep (typically at 250°C with a strain rate of 6.10^{-4} s^{-1}), and by grain boundary sliding (typically at 400°C with a strain rate of 6.10^{-4} s^{-1}). Finally, we have chosen the strain rate in order to obtain similar Z-parameters over the temperature range 200-300°C. This was achieved applying a strain rate of 5.10^{-5} s^{-1}. Note that room temperature deformation was not included in our analysis because of the profuse twinning activity detected under tension at room temperature. An additional constraint was imposed by preliminary observations: for strains larger than 0.15, dynamic recrystallization is likely to occur at 200°C making the comparison with tests run at 250 and 300°C impossible because of significant microstructure evolutions. Thus comparisons will be restricted to the tensile strain range 0-0.15.

2.3. Micromechanical characterization

Micro-tensile specimens with a width of 1.5 mm and a gauge length of 3 mm were extracted from the AZ31 as-received metal sheet with the tensile axis parallel to the rolling direction (RD). Subsequently, regions of interest were preliminarily characterized by EBSD. Fiducial microgrids made of gold were deposited using electron beam lithography over the region of interest (typically 100 x 100 µm) using a step size of 2 microns, see details in [19–21] regarding the microgrids deposition procedure. SEM imaging after every strain increment was performed at 15 kV using a definition of 4096 x 3072 pixels. Grayscale histograms were optimized by adjusting both contrast and brightness in order to achieve a maximum spread over the entire grayscale. Digital Image Correlation (DIC) was performed using the software CorrelManuV [19,21,22] to determine the microgrid intersection displacements. Microgrids presents also the advantage of revealing undoubtedly grain boundary sliding. More details are given in **Appendix A**.

2.4. Slip trace analysis

The activation of the various slip systems, namely basal, prism and pyramidal <c+a> during high-temperature tensile loading at 200, 250 and 300°C at a constant strain-rate of 5.10^{-5} s^{-1} was examined through an EBSD-assisted slip trace analysis consisting in:

(i) acquiring large EBSD maps in the gauge length of the micro tensile specimens in the undeformed conditions;

(ii) straining the samples to a macroscopic tensile strain of 0.10;

(iii) imaging the regions preliminary mapped by EBSD using SE-contrast using low voltage 5kV.

The assignment of each slip trace observed in the SEM-SE images to a given slip system was carried out using the Euler angles as inputs into a Matlab routine, which provide as outputs the angular deviation in comparison to the theoretical plane traces of every slip system. In most cases, only one set of slip traces was detected in a given grain. The identification of the slip system activated based on the slip trace was considered when the two following conditions were satisfied:

- the angular deviation between the theoretical plane trace and the experimental slip trace must be lower than 5°;
- only one slip system shows an angular deviation lower than 5°. In other words, it was considered that if two or more slip system have an angular deviation < 5°, then the slip trace could not be unambiguously identified.

Note that pyramidal <a> systems could not be easily identified because a combination of basal and prismatic <a> cross slip gives the same trace as pyramidal <a> slip [23].

3. Identification of the deformation mechanisms

3.1. Rheology

To characterize the rheology of the fine grained AZ31 alloy at high temperatures, both sets of mechanical testing were carried out.

First, strain-rate controlled in situ high-temperature tensile tests were conducted at 200, 250 and 300°C at 5.10^{-5} s^{-1}. Recording the true-stress/strain response during in situ tensile tests within the SEM is not straightforward, in particular, because no local extensometer attached to gauge length could be used to accurately measure the displacement, hence strain along the tensile direction. The tensile true-stress/strain response was extracted from the force measured by the load cell, and the average tensile strain calculated based on the local tensile strain measured at each grid intersection. An image was recorded at each strain increment that goes along with a stress release. To estimate the true stress, the force was recorded just before stress release. This methodology finally enables the full tensile response to be determined as illustrated in **Figure 2**. One can also look at the evolution of the mechanical anisotropy with temperature by calculating the Lankford coefficient, $r = \varepsilon_{width}/\varepsilon_{thickness}$. At room temperature, the Lankford coefficient with values close to 4 is usually reported [1,2]. Plastic anisotropy is strongly reduced when increasing temperature: r becomes closer to 1.4 at 200°C and tends towards 1 at 250°C and 300°C. Again those results were found to be consistent with what is currently reported in the literature, see e.g. [1,2].

Second, in situ SEM high-temperature tensile tests, also performed at 200, 250 and 300°C, were carried out to evaluate the strain rate sensitivity by applying abrupt strain rate changes. The strain rate sensitivity index, m was calculated as follows: $m = \ln(\sigma_2/\sigma_1)/\ln(\varepsilon_2/\varepsilon_1)$. At 200°C, $m \approx 0.2$ suggesting that dislocation creep was the predominant deformation mechanism. At both 250 and 300°C, $m \approx 0.5$ supporting the idea that a significant contribution of grain boundary sliding (GBS) is expected. Those values are consistent with the strain-rate sensitivity reported in [24–26][9][27][28] for the same alloy exhibiting grain size of the same order of magnitude. Thus those results demonstrate that our experimental device enables to properly identify the rheology of the investigated material.

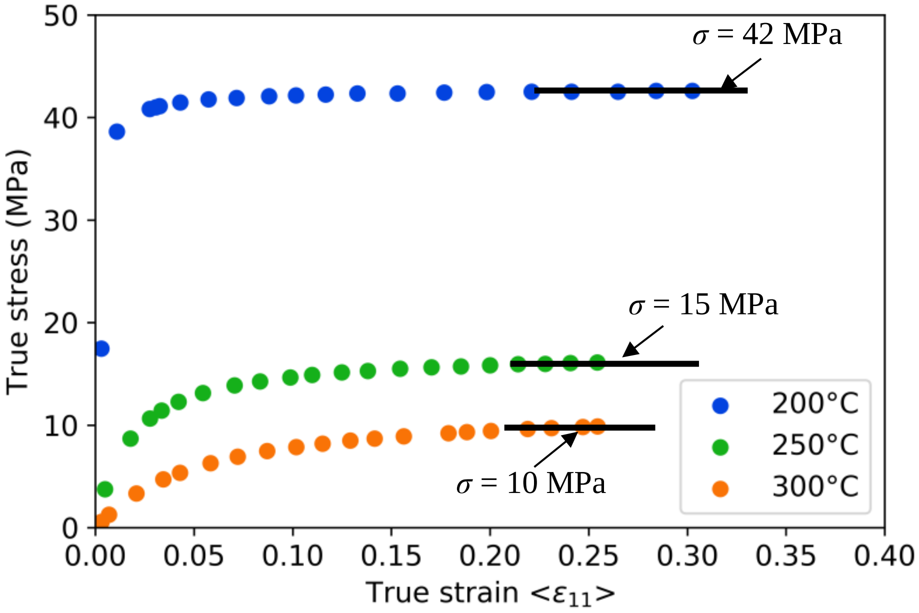

Figure 2. Tensile true stress-strain responses determined at 200, 250 and 300°C at 5.10^{-5} s^{-1} from in situ tensile tests.

3.2.Microstructural observations: SEM and EBSD

3.2.1. Coexistence of deformation mechanisms

SEM observations of the region covered by the microgrids allow identifying several deformation mechanisms operating during high-temperature deformation of the AZ31 Mg-alloy. At each temperature, a coexistence of the deformation mechanisms is detected, see example in **Figure 3**. Though the strain-rate sensitivity was found to be significantly different, i.e. $m \approx 0.2$ at 200°C and $m \approx 0.5$ at 250°C and 300°C, GBS was evidenced by the microgrids at 200°C and intragranular deformation was also observed in some grains at 300°C. Note that grain rotation was often observed to go along with GBS. This terminology here must be used carefully because it does not mean conventional crystallographic lattice rotation induced by dislocation slip but it is rather a rigid body rotation. More quantitative considerations will be suggested and discussed in section 4.

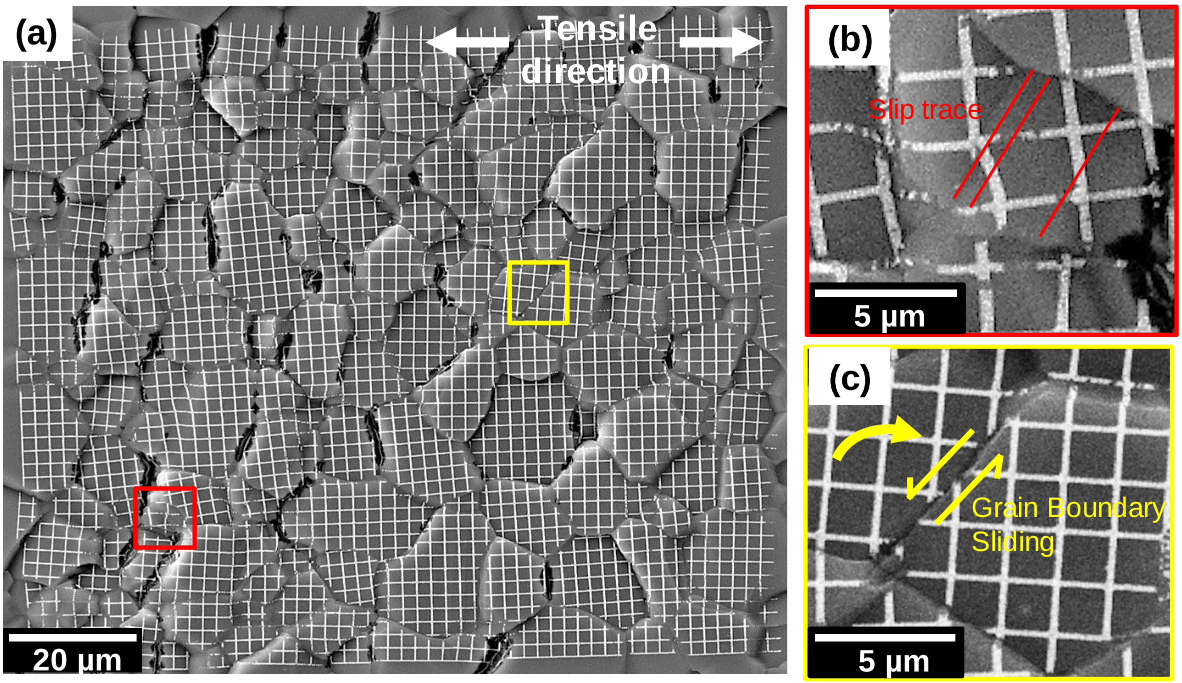

Figure 3. (a) SEM-SE micrograph of the deformed microgrids: T = 250°C and $<\varepsilon_{11}>$ = 0.15 (Tensile direction is parallel to RD). (b)-(d) Enlarged views illustrating the coexistence of different deformation mechanisms: (a) dislocation glide with slip traces, (c) grain boundary sliding. Note that grain boundary sliding is often observed to go along with rigid body rotation.

3.2.2. Recrystallization and grain growth

In addition to the SEM images taken at every strain increments, EBSD maps were acquired at the end of the tensile tests in order to investigate the possible microstructural evolutions during high temperature tensile testing. Large areas were characterized to ensure the statistical consistency of the results. Tests were stopped at a strain of 0.30. Deformed samples were therefore re-polished to make the surface suitable for further EBSD analysis, see **Figure 4**. At 200°C, two features have drawn our attention:

(i) finer grains (9 µm) were observed in **Figure 4b** in comparison with what was measured in the as-received microstructure (12 µm), see **Figure 4a**. Note that strictly the same definition of the grain size was systematically used to avoid any biased measurements.

(ii) the morphology of the grain boundaries had evolved: from straight interfaces in the as-received conditions to more concave or convex shape after 0.3 overall tensile strain indicating the migration of grain boundaries.

At 250 and 300°C, the observed microstructural evolutions were very similar: the average grain size was slightly larger: 15 and 16 µm at 250 and 300°C (**Figure 4c**) respectively vs. 12 µm in the as-received conditions. Those results were confirmed using the model developed by Del Valle et al. [29] allowing to estimate the recrystallized grain size (d_{RX}) based on the determination of the flow stress (σ) measured at a given temperature and strain rate: $d_{RX} = 5400/\sigma^{1.57}$. This model was established based on various tensile mechanical tests run at different temperatures and strain rates. This model predicted a recrystallized grain size of 15, 81 and 205 µm at respectively 200, 250 and 300°C. Hence, it was concluded that DRX can occur at large strain at 200°C while it was not triggered at 250 and 300°C since very coarse recrystallized grain sizes were predicted by the model of Del Valle et al. [29]. At 250 and 300°C, only a slight grain growth was detected. As a result, it must be highlighted that the characterization and analyses done in the subsequent sections have been restricted to the plastic strain range 0-0.15 in order to avoid any significant microstructural evolution such as recrystallization. Indeed, when imaging the gridded region during in situ tensile tests, there was no sign of recrystallization up to 0.15 tensile strain, see e.g. **Figure S1**.

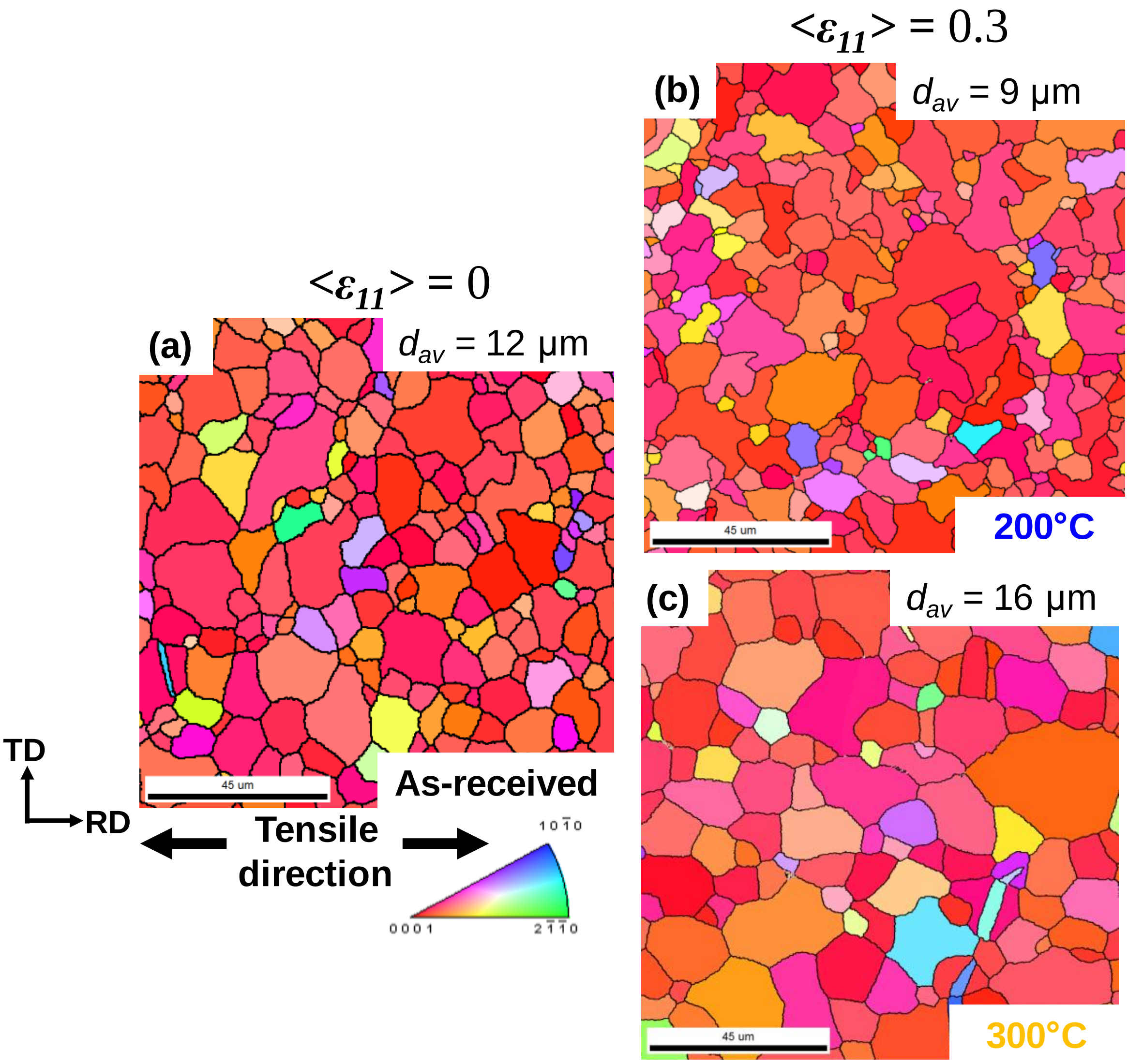

Figure 4. EBSD IPF-Z maps: (a) in the undeformed conditions ($<\varepsilon_{11}> = 0.0$); (b) and (c) after straining ($<\varepsilon_{11}> = 0.30$) for T = 200 and 300°C respectively.

3.3. *Dislocation activity: slip trace analysis*

At room temperature, basal slip is expected to be predominant whereas at high-temperature [4,7,30] other slip systems are expected to be activated [3,4,7]. To provide insights into the activation of the different slip systems, a slip trace analysis was carried out for samples strained to 0.1.

At each temperature (200, 250 and 300°C), we have identified at least 100 grains in which the active slip traces were unambiguously determined based on the rules described in section 2.4. The results are shown in **Figure 5**. Basal, prism and pyramidal <c+a> dislocations were detected at 200, 250 and 300°C. It means that for a strain rate of 5.10^{-5} s^{-1}, all the slip systems were activated. However, it seems very difficult to conclude regarding the relative contribution of the various slip systems as this methodology suffers from several issues that deserve to be commented on. One has to keep in mind that only the grains showing slip traces are analyzed, the others being ignored in the analysis. Many grains might be deformed by dislocation glide but slip traces cannot be detected because dislocations do not come out into the plane of observation. As explained in section 2.4, large areas were initially mapped by EBSD before straining at high-temperature. With the magnification used, approximately 1000 grains were contained within a map. At 200°C, we found clear slip traces in approximately 25% of the grains analyzed. At 250°C, roughly 20% of the grains observed contained slip traces. At 300°C, only 10% of the grains analyzed contained well-distinguishable slip traces.

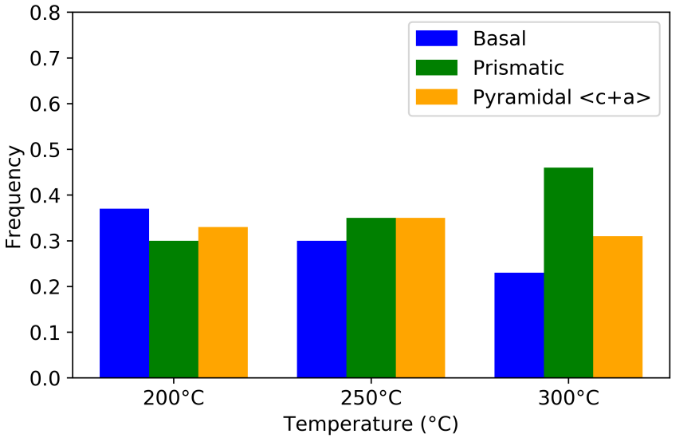

Figure 5. Comparison of the active slip systems at 200, 250 and 300°C based on the slip trace analysis.

Very few experimental studies have been focused on the identification of the relative contributions of the different slip systems during high-temperature deformation of the AZ31 Mg-alloy in the literature, see [7,31–33]. Boehlert et al. [7] performed tensile tests at 50, 150 and 250°C at ≈ 10^{-3} s^{-1} along the RD direction on an AZ31 rolled sheet with a grain size of 13 µm, very similar to the material studied here. They found that at 250°C, the main activated systems were the basal and prismatic systems with a substantial predominance of the prismatic one while the pyramidal <c+a> activity was almost inactive. Interestingly, in our case, even at 200°C it is rather clear that all the slip systems are activated. The latter result is not fully consistent with the results reported by Barnett et al. in [3] which suggests that at 200°C basal slip is still predominant. This difference with the results published by Barnett et al. in [3] could be explained by a difference in strain rate. In the present work, a rather slow strain rate was employed (5.10^{-5} s^{-1}). To fully unravel the possible effect of strain-rate on the contribution of the different slip systems would require several additional tests and characterizations and this was considered out of the scope of the present study. For instance, comparing slip trace analysis results under different conditions (temperature and strain rates) would require to ensure that the exact same methodology is employed: statistics but also the requirements set to identify with a high confidence the operating slip system. The most striking result here is that upon 200°C, the different slip systems are already activated and that basal slip does not seem the predominant deformation mechanism.

3.4. Grain Boundary Sliding (GBS)

In situ tensile tests enable us to provide insights into the GBS mechanism since the grain boundaries affected by GBS can be identified and follow throughout the tensile testing. A typical example is shown in **Figure 6a** where GBS is evidenced with the help of fiducial microgrids. Those observations suggest that GBS is a continuous process and does not occur through a two-steps discontinuous stick and slide mechanism. The presence of the microgrids allows reflecting more quantitatively this continuous mechanism. For several grains undoubtedly affected by GBS, the displacement parallel to the tensile direction as defined in **Figure 6a** was estimated after different strain increments. The evolution of ΔL was then plotted with strain in **Figure 6b** for those grains, confirming the continuous character of GBS relying on the microgrids offsets.

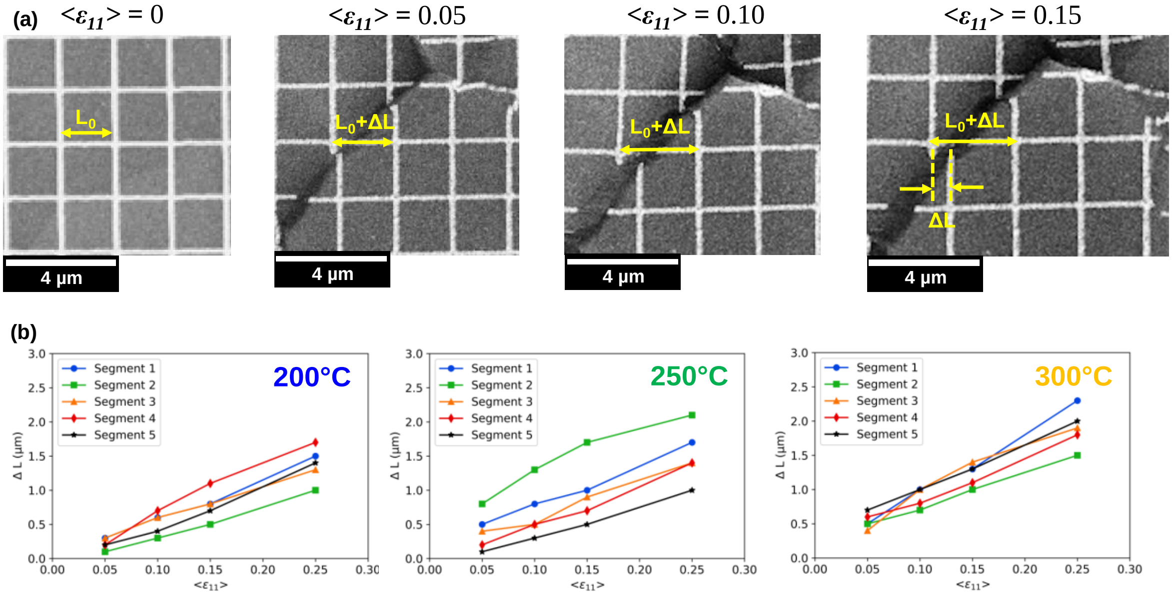

Figure 6. (a) Observations of GBS during in situ high-temperature tensile loading evidenced by micrograds displacements: typical example at 200°C. (b) Evolution of the displacement induced by GBS along several GB unambiguously identified to be affected by GB.

We also aimed at observing qualitatively the effect of temperature on the overall activity of GBS. As highlighted before, at each temperature: GBS was evidenced by grid line offsets. However, GBS activity is expected to differ significantly as a function of temperature [13,34]. This can be nicely illustrated by looking at enlarged views of the SEM images taken after different strain increments at different temperatures as shown in **Figure 7**. One can see major differences when observing the microgrids within grains and in the neighborhood of grain boundaries, in particular at 250°C and 300°C. At 200°C, many grains exhibit a distorted microgrid in their core (**Figure 7a**) while at both 250 and 300°C the microgrid is still undeformed within grains (square grids remain after straining). At both 250 and 300°C, GBS seems to occur along the majority of GBs (**Figure 7b-c**) whereas it is limited to a few GBs at 200°C. Interestingly, GBS is very often assisted by grain rotation (rigid body rotation). High definition SEM-images of the whole deformed microgrids after different strain increments and at 200, 250 and 300°C are also given as supplementary materials, see **Figure S1-S3**. Videos illustrating the occurrence of GBS at 250 and 300°C are also provided as supplementary materials, see **Video S1** (250°C) and **Video S2** (300°C).

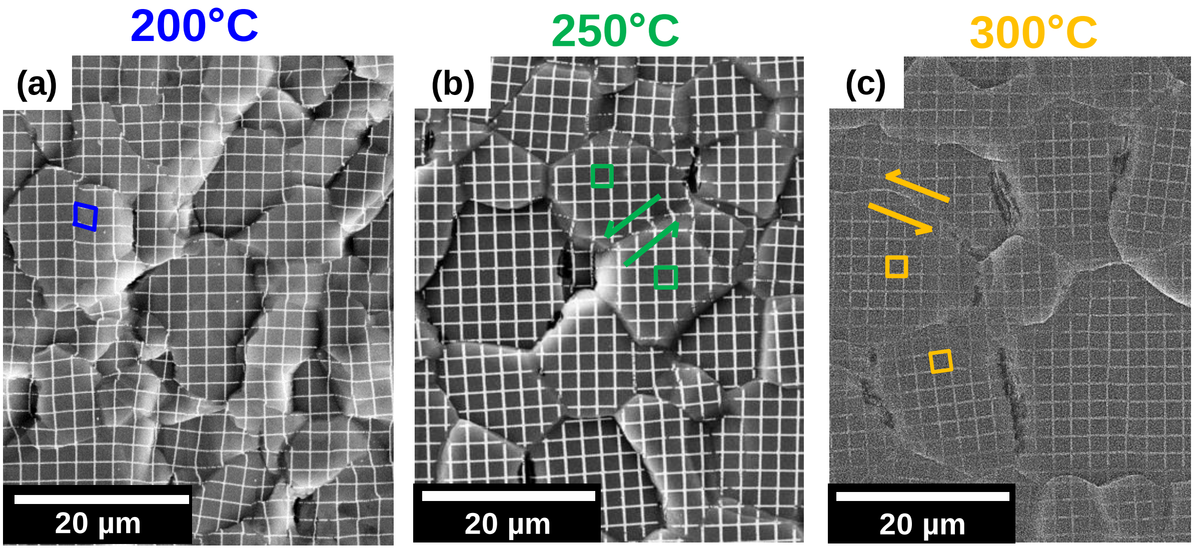

Figure 7. SEM-SE micrographs of the microgrids taken after a macroscopic tensile strain of $<\varepsilon_{11}>$ = 0.10 at: (a) 200°C; (b) 250°C and (c) 300°C. Note that images taken at 300°C exhibit a limited contrast because those images were acquired under the VPSE mode while at 200 and 250°C the HV mode was employed. Arrows indicate grain boundary sliding while symbols illustrate schematically grid evolution within grains. Note that GBS affects most of the grain boundaries at 250 and 300°C but is restricted to a few boundaries at 200°C.

4. Spatial distribution of plastic strain heterogeneities with temperature

4.1. Effect of macroscopic tensile strain

We first looked at the effect of strain on the development of deformation heterogeneities by plotting strain maps after different strain increments. An example is given in **Figure 8** where the spatial strain heterogeneity at 300°C within the region containing the microgrid is plotted for various macroscopic tensile strain. The strains calculated by DIC are represented as color maps corresponding to the magnitude of the normalized equivalent strain: $\varepsilon_{eq}/<\varepsilon_{eq}>$. The normalized equivalent strain is calculated as the ratio between the local equivalent strain measured at each grid intersection over the average equivalent strain calculated over the whole gridded region. Also shown in **Figure 8** are the location of the grain boundaries (misorientation > 5°).

Significant strain heterogeneities can be observed with some regions exhibiting local strains up to five times larger than the macroscopic strain and other regions almost undeformed. Interestingly, the strain heterogeneities develop at low plastic strain and do not evolve significantly with strain as illustrated in **Figure 8**. This also stands at 200 and 250°C, see **Figure S4** in supplementary materials. In other words, it is sufficient to focus on one level of macroscopic strain for further analysis.

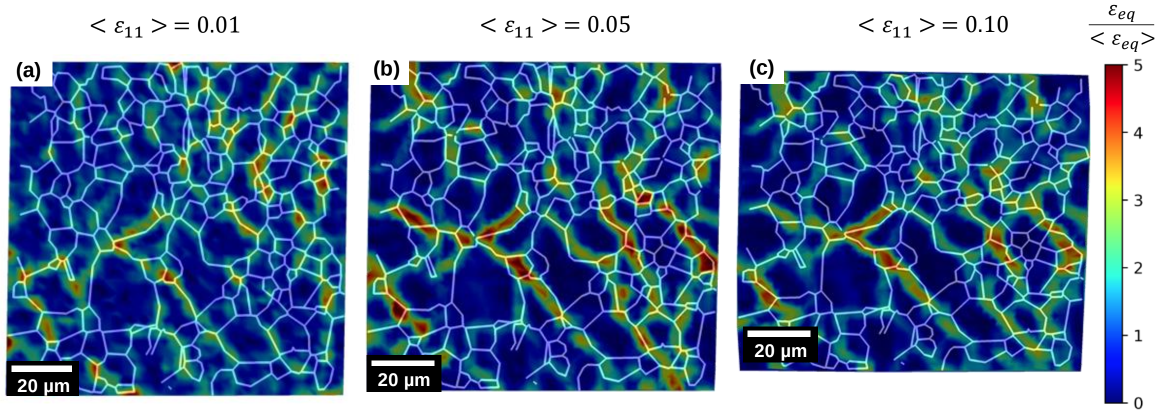

Figure 8. Normalized equivalent strain maps ($\varepsilon_{eq}/<\varepsilon_{eq}>$) for a sample deformed at 300°C for different macroscopic tensile strain: (a) $<\varepsilon_{11}> = 0.01$; (b) $<\varepsilon_{11}> = 0.05$ and (c) $<\varepsilon_{11}> = 0.10$.

4.2. Effect of temperature

When examining strain maps at different temperatures at a given macroscopic strain, strain amplification occurs in the vicinity of grain boundaries, see **Figure 9**. Whatever the temperature, strain amplification occurs at GBs. Large strains are often found close to GB whereas low strains are rather located within grains. This is better reflected by plotting strain maps with suitable scale bars as shown in **Figure S5**. An in-depth analysis is now required to evaluate the effect of temperature on the strain amplification along GBs, this is the purpose of the following section.

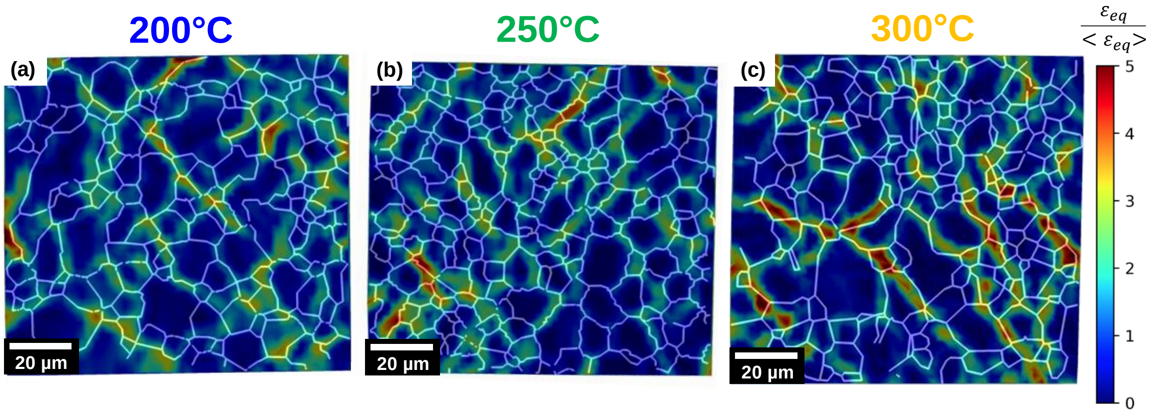

Figure 9. Normalized equivalent strain maps ($\varepsilon_{eq}/<\varepsilon_{eq}>$) for a macroscopic tensile strain of $<\varepsilon_{11}> = 0.05$ at (a) 200°C; (b) 250°C and (c) 300°C.

4.3. Strain localization in the vicinity of grain boundaries

4.3.1. Evaluating strain amplitude near GBs

To evaluate whether there is an effect of temperature on the strain localization in the vicinity of grain boundaries, the Euclidean distance between each grid intersection and the closest grain boundary was calculated, see **Figure 10a-b**. To ensure the statistical consistency of the results, it was first assessed that the region of interest selected at each temperature exhibits a similar microstructure. To do so, the number of grid intersections in the immediate vicinity of GBs, i.e. intersections located within the interval [0;0.5[μm (**Figure 10b**) was determined for the region of interest selected at each temperature. **Table 1** gives the percentage of grid intersections located at a distance to grain boundary shorter than 0.5 microns. This demonstrates that the number of grid intersections located near GB does not change significantly over the region of interest selected at each temperature. In other words, it shows that the microstructure can be considered as relatively homogeneous from a sample to another. Because every gridded region contains 2500 grid intersections, it means that roughly one-quarter of the data points are located within the interval [0;0.5[μm.

200°C	250°C	300°C
21%	26%	25%

Table 1. % of grid intersections located in the interval [0;0.5] at each temperature.

Once the consistency of the microstructure has been assessed from one sample to another, the histogram showing the average normalized equivalent local strain as a function of the distance to GB has been plotted for a macroscopic strain of 0.10 for each temperature, see **Figure 10c**. Two conclusions can be drawn from **Figure 10c**:

(i) whatever the temperature, strain localization occurs in the vicinity of GBs (intergranular region): strain decreases when moving away from the grain boundaries.

(ii) the higher the temperature, the larger the strain localization in the vicinity of grain boundaries, and, inversely the lower the intragranular strain. The grid intersections located in the immediate vicinity of the grain boundaries deform twice more than the macroscopic strain at 300°C while it deforms only 1.2 times more at 200°C.

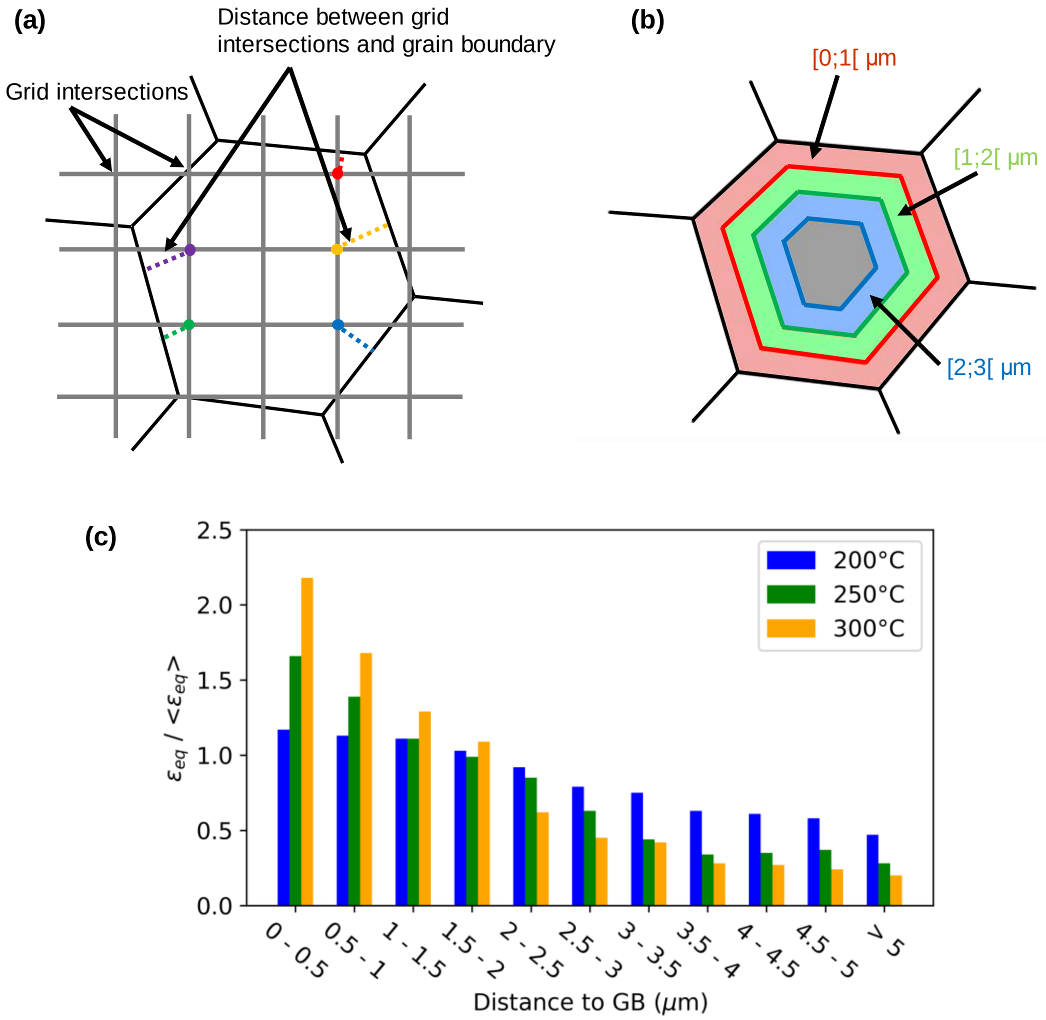

Figure 10. (a)-(b) Schematic illustrating the methodology used to evaluate the Euclidean distance between each grid intersection and grain boundaries. (c) Histogram showing the normalized equivalent strain ($\varepsilon_{eq}/<\varepsilon_{eq}>$) as a function of the Euclidean distance to grain boundary for a macroscopic strain of 0.10 at 200, 250 and 300°C.

The data points contained within the interval [0;0.5[µm are analyzed in more detail by plotting their strain distribution at 200, 250 and 300°C respectively, see **Figure 11a-c**. Note that on each strain histogram:

- a black line is plotted and corresponds to the average normalized equivalent strain within the interval [0;0.5[µm and corresponding to the average value reported in **Figure 10**;
- a gray dotted line is also added to distinguish data points with a normalized equivalent strain $\varepsilon_{eq}/<\varepsilon_{eq}> > 1$ from those having a ratio $\varepsilon_{eq}/<\varepsilon_{eq}> < 1$. In other words, these gray dotted lines help to discriminate points deforming more than the average equivalent strain over the region of interest from those deforming less.

Figure 11a-c reveals that when the temperature increases from 200°C to 300°C, the strain distribution of the grid intersections located within [0;0.5[µm is shifted towards larger strains. Thus points located near grain boundaries tend to deform to a larger extent when the temperature increases. This quantitative analysis is consistent with the observations made (i) on the SEM micrographs displayed in **Figure 7** (see also **Figure S1-S3**), and (ii) on the strain maps shown in **Figure 9** (see also **Figure S4** and **Figure S5**). Besides grid intersections located in the immediate vicinity of grain boundaries and deforming less than the macroscopic equivalent strain, i.e. $\varepsilon_{eq}/<\varepsilon_{eq}> < 1$, tend to disappear when increasing the temperature. On the contrary, raising the temperature leads to a substantial increase of the fraction of grid intersections deforming twice more than the macroscopic equivalent strain, i.e. $\varepsilon_{eq}/<\varepsilon_{eq}> > 2$. To summarize, it can be concluded that as the temperature increases, strain localization intensifies near grain boundaries.

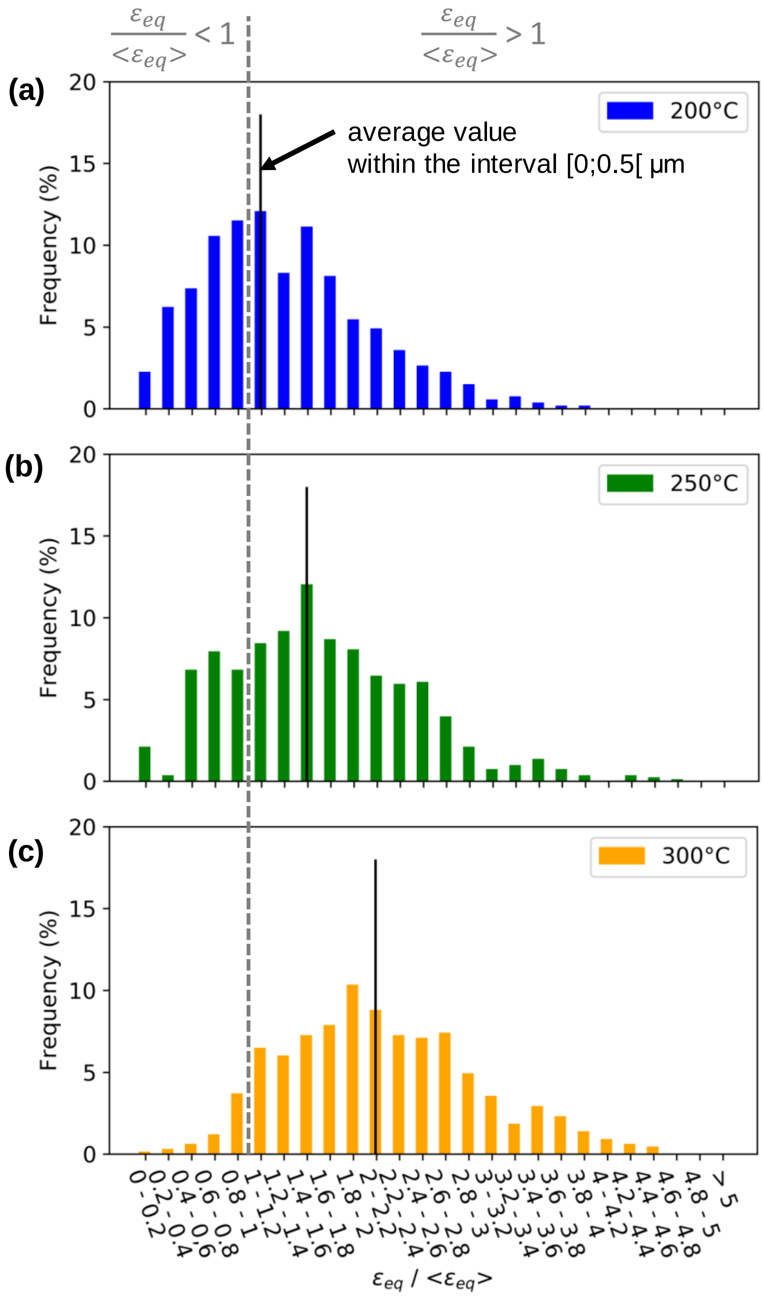

Figure 11. Histogram showing the local strain distribution for all grid intersections located at a distance between 0 and 0.5 microns from a grain boundary: (a) at 200°C: (b) at 250°C and (c) at 300°C. The black line corresponds to the average normalized equivalent strain in the interval [0; 0.5]. Gray dotted line helps to discriminate points deformation more than the average equivalent strain computed over the region of interest ($\varepsilon_{eq}/<\varepsilon_{eq}> > 1$) from those deforming less ($\varepsilon_{eq}/<\varepsilon_{eq}> < 1$).

4.3.2. Link between strain localization and grain boundary sliding

Whatever the temperature between 200 and 300°C, strain maps have shown that strain localization occurs preferentially in the vicinity of grain boundaries. However, with the spatial resolution of our DIC measurement it is difficult to conclude if this strain amplification is localized at the grain boundary or if it results from a larger slip activity in the vicinity of grain boundaries. This is further exemplified with the help of the schematics shown in **Figure 12a** and **Figure 12b**. Thus one has to be very careful when interpreting such results because strain localization at grain boundaries is not necessarily the sign of the activation of GBS but might time-to-time result from localized slip activity (**Figure 12b**). This turns out to be particularly true at 200°C where dislocation glide is expected to be predominant over GBS (strain rate sensitivity index *m* close to 0.2). On the contrary, samples strained at 250°C and 300°C at 5.10^{-5} s^{-1} are deformed under superplastic conditions as shown by the strain sensitivity index *m* found to be close to 0.5. This is also consistent with the microgrids observations made at 250°C and 300°C which reveal a lot of occurrences of grain boundary sliding, see **Figure 7b-c**. Under superplastic conditions (250 and 300°C), strain localization at grain boundaries can, in most of the cases, be considered as the signature of the occurrence of GBS as nicely revealed by microgrids, see typically **Figure 7b-c**.

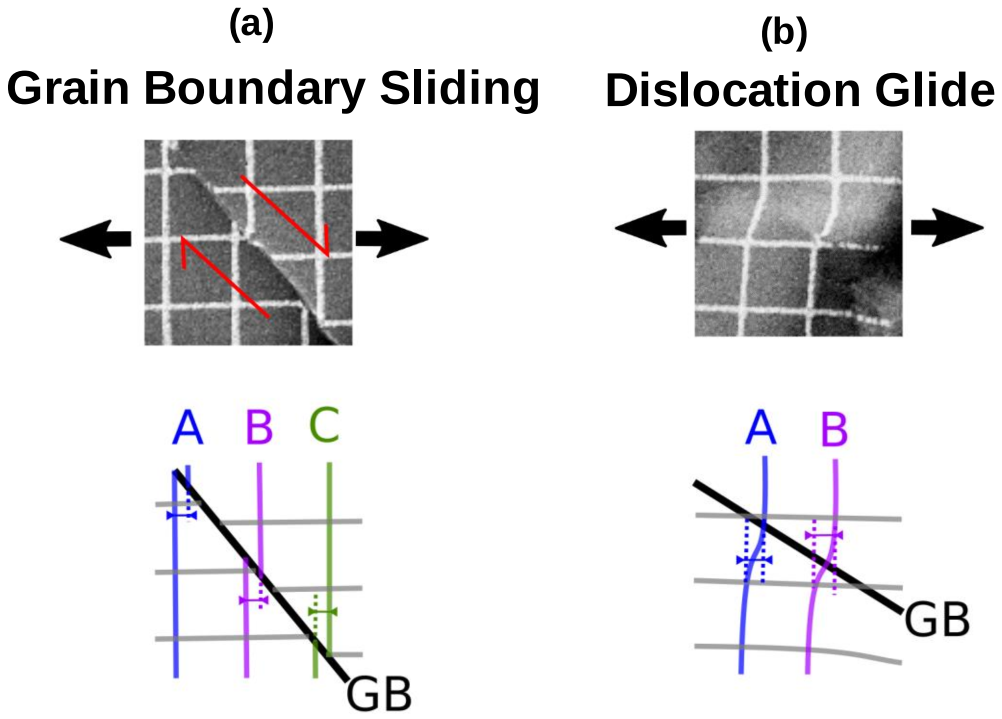

Figure 12. Illustration of the typical deformation mechanisms as revealed by the microgrids and observed in the vicinity of grain boundaries during high temperature straining. (a) Grain Boundary Sliding. Schematics are drawn to help the reader discriminating both deformation mechanisms. (b) Dislocation glide.

5. Conclusions

The main conclusions emerging from the present work can be drawn as follows:

- A specific environment has been developed to conduct in situ strain-rate controlled high-temperature tensile tests within the SEM of Mg-alloys. This set-up was coupled with EBSD and DIC measurements allowing to provide new insights into the deformation mechanisms and the development of microscale strain heterogeneities as a function of temperature.
- Dislocation creep and grain boundary sliding (GBS) coexist between 200 and 300°C.
- Prismatic and pyramidal slip were already active at 200°C.
- GBS mechanism occurs continuously and not in a stick-and-slip way.
- Microscale strain heterogeneities develop from the first stages of plastic deformation and persist at larger strains.
- When the temperature increases from 200 to 300°C, strain localization near GBs increases (in agreement with change in strain-rate sensitivity *m* values), while the core of the grains accommodates less deformation.
- Our measurement of strain amplification near GBs based on the microgrid displacements is not necessarily the signature of GBS, in particular at 200°C.

Acknowledgements

This work was performed within the framework of the Center of Excellence of Multifunctional Architectured Materials ‘‘CEMAM’’ n°AN-10-LABX-44-01 funded by the ‘‘Investments for the Future Program’’. Doctoral school I-MEP2 is gratefully acknowledged for funding.

Data Availability

The raw/processed data required to reproduce these findings cannot be shared at this time due to technical or time limitations.

References

[1] M.R. Barnett, A. Ghaderi, I. Sabirov, B. Hutchinson, Role of grain boundary sliding in the anisotropy of magnesium alloys, Scr. Mater. 61 (2009) 277–280. doi:10.1016/j.scriptamat.2009.04.001.

[2] N. Stanford, K. Sotoudeh, P.S. Bate, Deformation mechanisms and plastic anisotropy in magnesium alloy AZ31, Acta Mater. 59 (2011) 4866–4874. doi:10.1016/j.actamat.2011.04.028.

[3] M.R. Barnett, A Taylor model based description of the proof stress of magnesium AZ31 during hot working, Metall. Mater. Trans. A Phys. Metall. Mater. Sci. 34 A (2003) 1799–1806. doi:10.1007/s11661-003-0146-5.

[4] A. Chapuis, J.H. Driver, Temperature dependency of slip and twinning in plane strain compressed magnesium single crystals, Acta Mater. 59 (2011) 1986–1994. doi:10.1016/j.actamat.2010.11.064.

[5] A. Jäger, P. Lukáč, V. Gärtnerová, J. Bohlen, K.U. Kainer, Tensile properties of hot rolled AZ31 Mg alloy sheets at elevated temperatures, J. Alloys Compd. 378 (2004) 184–187. doi:10.1016/j.jallcom.2003.11.173.

[6] G. Ayoub, A.K. Rodrigez, M. Shehadeh, G. Kridli, J.P. Young, H. Zbib, Modelling the rate and temperature-dependent behaviour and texture evolution of the Mg AZ31B alloy TRC sheets, Philos. Mag. 98 (2018) 262–294. doi:10.1080/14786435.2017.1403054.

[7] C.J. Boehlert, Z. Chen, I. Gutiérrez-Urrutia, J. Llorca, M.T. Pérez-Prado, In situ analysis of the tensile and tensile-creep deformation mechanisms in rolled AZ31, Acta Mater. 60 (2012) 1889–1904. doi:10.1016/j.actamat.2011.10.025.

[8] Y. Liu, P. Mao, F. Zhang, Z. Liu, Z. Wang, Effect of temperature on the anisotropy of AZ31 magnesium alloy rolling sheet under high strain rate deformation, Philos. Mag. 98 (2018) 1068–1086. doi:10.1080/14786435.2018.1427896.

[9] W.J. Kim, S.W. Chung, C.S. Chung, D. Kum, Superplasticity in thin magnesium alloy sheets and deformation mechanism maps for magnesium alloys at elevated temperatures, Acta Mater. 49 (2001) 3337–3345. doi:10.1016/S1359-6454(01)00008-8.

[10] H. Somekawa, K. Hirai, H. Watanabe, Y. Takigawa, K. Higashi, Dislocation creep behavior in Mg-Al-Zn alloys, Mater. Sci. Eng. A. 407 (2005) 53–61. doi:10.1016/j.msea.2005.06.059.

[11] J.A. del Valle, F. Peñalba, O.A. Ruano, Optimization of the microstructure for improving superplastic forming in magnesium alloys, Mater. Sci. Eng. A. 467 (2007) 165–171. doi:10.1016/j.msea.2007.02.088.

[12] R. Panicker, A.H. Chokshi, R.K. Mishra, R. Verma, P.E. Krajewski, Microstructural evolution and grain boundary sliding in a superplastic magnesium AZ31 alloy, Acta Mater. 57 (2009) 3683–3693. doi:10.1016/j.actamat.2009.04.011.

[13] M. Kawasaki, R.B. Figueiredo, T.G. Langdon, The Requirements for Superplasticity with an Emphasis on Magnesium Alloys, Adv. Eng. Mater. 18 (2016) 127–131. doi:10.1002/adem.201500068.

[14] P. Lhuissier, M. Scheel, L. Salvo, M. Di Michiel, J.J. Blandin, Continuous characterization by X-ray microtomography of damage during high-temperature deformation of magnesium alloy, Scr. Mater. 69 (2013) 85–88. doi:10.1016/j.scriptamat.2013.03.001.

[15] R. Boissière, Effet de la température sur les capacités de mise en forme d’alliages de magnésium corroyés, Grenoble INP, 2008. http://www.theses.fr/2008INPG0104.

[16] A. Orozco-Caballero, D. Lunt, J.D. Robson, J. Quinta da Fonseca, How magnesium accommodates local deformation incompatibility: A high-resolution digital image correlation study, Acta Mater. 133 (2017) 367–379. doi:10.1016/j.actamat.2017.05.040.

[17] G. Martin, C.W. Sinclair, J.H. Schmitt, Plastic strain heterogeneities in an Mg-1Zn-0.5Nd alloy, Scr. Mater. 68 (2013) 695–698. doi:10.1016/j.scriptamat.2013.01.017.

[18] C.C. Aydiner, M.A. Telemez, Multiscale deformation heterogeneity in twinning magnesium investigated with in situ image correlation, Int. J. Plast. 56 (2014) 203–218. doi:10.1016/j.ijplas.2013.12.001.

[19] G. Martin, C.W. Sinclair, R.A. Lebensohn, Microscale plastic strain heterogeneity in slip dominated deformation of magnesium alloy containing rare earth, Mater. Sci. Eng. A. 603 (2014) 37–51. doi:10.1016/j.msea.2014.01.102.

[20] T. Dessolier, G. Martin, P. Lhuissier, C. Josserond, F. Roussel, F. Charlot, J.-J. Blandin, L. Maniguet, Conducting Controlled In Situ High Temperature Tensile Tests within a SEM, Microsc. Anal. (2018). https://microscopy-analysis.com/article/july_18/High_Temperature_Tensile_Testing_in_situ.

[21] L. Allais, M. Bornert, T. Bretheau, D. Caldemaison, Experimental characterization of the local strain field in a heterogeneous elastoplastic material, Acta Metall. Mater. 42 (1994) 3865–3880.

[22] G. Martin, D. Caldemaison, M. Bornert, C. Pinna, Y. Bréchet, M. Véron, J.D. Mithieux, T. Pardoen, Characterization of the High Temperature Strain Partitioning in Duplex Steels, Exp. Mech. 53 (2013). doi:10.1007/s11340-012-9628-y.

[23] S.R. Agnew, C.N. Tomé, D.W. Brown, T.M. Holden, S.C. Vogel, Study of slip mechanisms in a magnesium alloy by neutron diffraction and modeling, Scr. Mater. 48 (2003) 1003–1008. doi:10.1016/s1359-6462(02)00591-2.

[24] J.A. Del Valle, M.T. Pérez-Prado, O.A. Ruano, Deformation mechanisms responsible for the high ductility in a Mg AZ31 alloy analyzed by electron backscattered diffraction, Metall. Mater. Trans. A Phys. Metall. Mater. Sci. 36 (2005) 1427–1438. doi:10.1007/s11661-005-0235-8.

[25] J. Koike, R. Ohyama, T. Kobayashi, M. Suzuki, K. Maruyama, Grain-Boundary Sliding in AZ31 Magnesium Alloys at Room Temperature to 523 K, Mater. Trans. 44 (2005) 445–451. doi:10.2320/matertrans.44.445.

[26] F.K. Abu-Farha, M.K. Khraisheh, Analysis of superplastic deformation of AZ31 magnesium alloy, Adv. Eng. Mater. 9 (2007) 777–783. doi:10.1002/adem.200700155.

[27] H. Somekawa, H. Watanabe, T. Mukai, K. Higashi, Low temperature diffusion bonding in a superplastic AZ31 magnesium alloy, Scr. Mater. 48 (2003) 1249–1254. doi:10.1016/s1359-6462(03)00054-x.

[28] T.J. Lee, Y.B. Park, W.J. Kim, Importance of diffusional creep in fine grained Mg-3Al-1Zn alloys, Mater. Sci. Eng. A. 580 (2013) 133–141. doi:10.1016/j.msea.2013.04.061.

[29] J.A. del Valle, O.A. Ruano, Influence of texture on dynamic recrystallization and deformation mechanisms in rolled or ECAPed AZ31 magnesium alloy, Mater. Sci. Eng. A. 487 (2008) 473–480. doi:10.1016/j.msea.2007.11.024.

[30] H. Wang, C.J. Boehlert, Q.D. Wang, D.D. Yin, W.J. Ding, In-situ analysis of the tensile deformation modes and anisotropy of extruded Mg-10Gd-3Y-0.5Zr (wt.%) at elevated temperatures, Int. J. Plast. 84 (2016) 255–276. doi:10.1016/j.ijplas.2016.06.001.

[31] C.M. Cepeda-Jiménez, J.M. Molina-Aldareguia, F. Carreño, M.T. Pérez-Prado, Prominent role of basal slip during high-temperature deformation of pure Mg polycrystals, Acta Mater. 85 (2015) 1–13. doi:10.1016/j.actamat.2014.11.013.

[32] C.M. Cepeda-Jiménez, J.M. Molina-Aldareguia, M.T. Pérez-Prado, Origin of the twinning to slip transition with grain size refinement, with decreasing strain rate and with increasing temperature in magnesium, Acta Mater. 88 (2015) 232–244. doi:10.1016/j.actamat.2015.01.032.

[33] C.J. Boehlert, Z. Chen, A. Chakkedath, I. Gutiérrez-Urrutia, J. Llorca, J. Bohlen, S. Yi, D. Letzig, M.T. Pérez-Prado, In situ analysis of the tensile deformation mechanisms in extruded Mg-1Mn-1Nd (wt%), Philos. Mag. 93 (2013) 598–617. doi:10.1080/14786435.2012.725954.

[34] T.G. Langdon, Grain boundary sliding revisited: Developments in sliding over four decades, J. Mater. Sci. 41 (2006) 597–609. doi:10.1007/s10853-006-6476-0.